Grazing incident small angle x-ray scattering study of polymer thin films with embedded ordered nanometer cells

Hideaki Yokoyama,[a] Cedric Dutriez, and Lei Li
Nanotechnology Research Institute, National Institute of Advanced Industrial Science and Technology, 1-1-1, Higashi, Tsukuba, Ibaraki 305-0035, Japan

Taichi Nemoto and Kenji Sugiyama
Department of Organic and Polymeric Materials, Graduate School of Science and Engineering, Tokyo Institute of Technology, 2-12-1, Ohokayama, Meguro-ku, Tokyo 152-8552, Japan

Sono Sasaki, Hiroyasu Masunaga, and Masaki Takata[b]
Japan Synchrotron Radiation Research Institute (JASRI), 1-1-1, Kouto, Sayo-cho, Sayo-gun, Hyogo 679-5198 Japan

Hiroshi Okuda
International Innovation Center, Kyoto University, Sakyo-ku, Kyoto 606-8501 Japan

Analysis of nanostructures is of increasing importance with advances of nanotechnology. Embedded nanostructures in thin films in particular are of recent interest. Grazing incident small angle x-ray scattering (GISAXS) has been recognized to be a powerful method to probe such embedded nanostructures; however, quantitative analysis of scattering pattern is not always trivial due to complex refraction and reflection at surface and interfaces. We prepared nanocellular thin films using block copolymer template with carbon dioxide (CO_2); CO_2 "bubbles" were formed in the CO_2-philic block domains. Such nanocellular structures were analyzed by GISAXS and simulated using distorted wave Born approximation (DWBA). Unlike traditional transmission x-ray scattering, GISAXS requires a careful choice of incident angle to analyze the form factor of scatters embedded in a thin film. Nevertheless, the GISAXS measurements under optimized geometry with quantitative calculations using DWBA revealed that the nanocells are spherical and aligned in a single layer of hexagonal lattice and are surrounded by CO_2-philic block domains. © 2007 American Institute of Physics. [DOI: 10.1063/1.2749724]

I. INTRODUCTION

We have recently succeeded to introduce closed empty nanometer cells (nanocells) in polymers using block copolymer template and supercritical carbon dioxide (scCO$_2$). Since the detail of the process has been published elsewhere,[1–4] we just briefly review the process. scCO$_2$ process is a well known method to introduce cells (bubbles) into polymeric materials. However, the cell size is typically of the order of micron or above since reducing the size of cells to 100 nm or below will cost a huge energetic penalty associated with the large surface area of such small cells. In order to overcome such an energetic barrier and to make cells smaller, artificial nuclei of cells are necessary. Block copolymers have been recognized as one of materials which self-assemble into a variety of nanostructures. In order to localize CO_2 within polymeric materials under CO_2 pressure, the CO_2-philic-block domains such as those of fluorinated blocks work very effectively as nuclei. By depressurizing at a reduced temperature to prevent the microcells from

forming, the trapped CO_2 creates nanometer cells of the order of 10 nm in the CO_2-philic domains.

While such unique fabrication of nanocells has been reported,[1–4] quantitative analysis of nanocellular structures in thin films has not been accomplished. The primary reason is that the nanocells are embedded in the film and the surface analytical tools are of no use. We reported a high throughput destructive method using reactive ion etching to remove the surface covering layer followed by scanning electron microscopy (SEM) and atomic force microscopy (AFM).[3,4] However, such analysis cannot accurately determine the size of cells, and a nondestructive quantitative method to analyze the size, shape, and spacing of nanocells is desired. Recently, grazing incident small angle x-ray scattering (GISAXS) has been recognized as a powerful technique to analyze thin films supported on substrates.[5–22] In this paper, we employ GISAXS to analyze the nanocellular structures in thin films fabricated by block copolymer templating with the CO_2 process. An emphasis is especially on the feasibility of the form factor analysis for two dimensionally ordered cell structures. The model calculation using distorted wave Born approximation (DWBA) is compared with the experiment to extract the size and shape of cells and the distribution of block chains around the cells.

---

[a]Electronic mail: yokoyama@ni.aist.go.jp
[b]Also at The RIKEN Harima Institute, 1-1-1, Kouto, Sayo-cho, Sayo-gun, Hyogo 679-5148, Japan.

TABLE I. Characterization of PS-PFMA and PS.

Code	M_w (PS)	M_w (PFMA)	M_w/M_n
PS-PFMA	20 000	13 000	1.10
PS	4 500	⋯	1.03

II. EXPERIMENT AND THEORY

A. Synthesis of block copolymers

A series of poly[styrene-*block*-(perfluorooctylethyl) methacrylate] (PS-PFMA) were polymerized by a sequential living anionic polymerization. First, styrene was polymerized in tetrahydrofuran at −78 °C with *sec*-butyllithium as an initiator under a high vacuum. The living polystyryllithium was capped with 1,1-diphenylethylene, and subsequently reacted with 2-perfluorooctylethyl methacrylate in the presence of lithium chloride. The detail of the synthesis, polymerization and characterization has been described elsewhere.[23] The molecular weight of the PS block was determined by size-exclusion chromatography with PS standards. The weight fraction of the PFMA block was measured by ^{1}H NMR, and the total molecular weight was calculated. The homopolystyrene was purchased from Polymer Source Inc. and used as received. The results of the characterization of PS-PFMA and PS are listed in Table I.

B. Preparation of nanocellular thin films

PS-PFMA block copolymer and PS homopolymer were dissolved in a (4:1) mixture of toluene and 1,1,1,3,3,3-hexafluoro-2-propanol. Solutions with various concentration were spun coated on a silicon wafer to form thin films of ∼50-nm-thick. The ratio of PS in the mixture was adjusted to 35%. The block copolymer thin films supported on silicon wafers were placed in a high- pressure vessel and pressurized with carbon dioxide. A stainless steel high-pressure vessel for CO_2 process was connected to a high-pressure liquid chromatography pump (JASCO PU-2086 plus) with a cooling head and to a back-pressure regulator (JASCO SCF-Bpg). The films were swollen at 20 MPa of CO_2 at 60 °C for 1 h and cooled down to 0 °C to freeze the swollen structures. Then CO_2 pressure was reduced with a slow rate (0.5 MPa min^{-1}). Consequently, the empty cells were introduced as schematically shown in Fig. 1 and previously reported.[1–4]

C. Ellipsometry

An ellipsometer (JASCO M200 spectrometer) with incident wavelengths between 400 and 800 nm at an incident angle of 60° from the surface normal was used for thickness determination. The thickness was used as a parameter for DWBA analysis to fit the GISAXS intensities.

D. GISAXS

GISAXS experiments were conducted at BL-40B2 beamline of SPring-8 synchrotron facility. The generated white x rays were monochromatized using a fixed-exit double crystal monochromator to 0.15 nm and focused by a
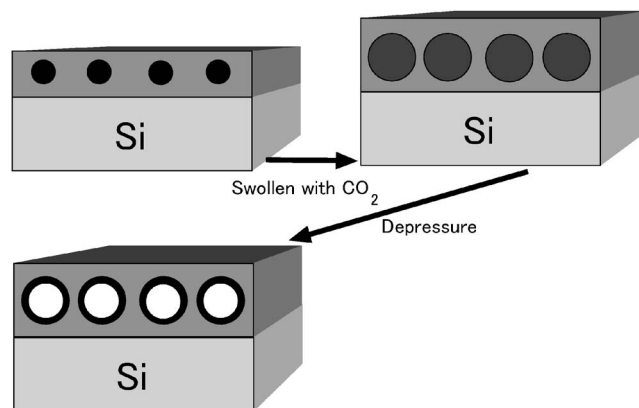

FIG. 1. Nanocellular formation using block copolymer template and CO_2 process. CO_2-philic block domains (shown as black) are swollen (dark gray) with CO_2 under CO_2 pressure. Temperature is quenched to 0 °C to freeze the non-CO_2-philic block domains (light gray). After depressurization, the empty cells (white) are introduced into the CO_2-philic block domains.

1-m-long rhodium-coated bent-cylinder mirror. A sample was placed in a vacuum chamber with Kapton windows on a computer controlled gonio stage. A schematic diagram of GISAXS geometry with coordinates used in this paper is shown in Fig. 2. The x-ray beam impinges at a small angle α_i onto a thin film supported on a substrate. In general, α_i is set to the vicinity of the critical angles of the thin film and substrate. The x-ray beam reflects/refracts, scatters, and reaches a two dimensional x-ray detector. An image intensifier accompanied with a charge coupled device (CCD) camera was used for two dimensional x-ray detection. A rectangular beam stopper (and/or copper attenuator) was placed to block the intense specularly reflected x ray. An incident angle was calibrated by the direct and specularly reflected x-ray positions on the detector. The incident angle of x ray on each sample was changed from 0.05° to 0.25°. The scattering angle was calibrated from the diffraction spots of collagen. The setup of GISAXS geometry at BL-40B2 beamline has been described elsewhere.[24]

E. Calculation of GISAXS intensities of thin films with ordered cells

1. Distorted wave Born approximation

We compute the small angle x-ray scattering intensities in GISAXS geometry using DWBA. The detail of DWBA has been described elsewhere[5–18,25,26] and we briefly review
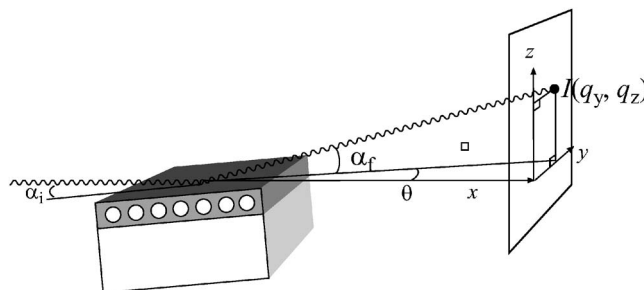

FIG. 2. Schematic picture of GISAXS geometry. x is defined as the directions of x ray. y and z are horizontal and vertical directions.

DWBA and show the scheme used to obtain the GISAXS intensities as a function of q_y and q_z. Scattering vectors are given by

$$q_x = \frac{2\pi}{\lambda}(\cos\theta\cos\alpha_f - \cos\alpha_i), \tag{1}$$

$$q_y = \frac{2\pi}{\lambda}\sin\theta\cos\alpha_f, \tag{2}$$

$$q_z = \frac{2\pi}{\lambda}(\sin\alpha_f + \sin\alpha_i), \tag{3}$$

where λ is the wavelength of x ray. We define the incident vertical angle α_i, the exit vertical angle α_f, and the exit horizontal angle θ as illustrated in Fig. 2 when the incident horizontal angle is zero. Since $\cos\alpha_f$ is close to unity in a small angle, the in-plane vector component q_y represents the in-plane structure. The vertical vector component q_z mainly provides the information in structure in the depth direction.

We assume a film with multiple layers, in which scattering densities are homogeneous, on a substrate. When an x-ray beam enters into the film, the beam refracted and reflected at each interface depending on the refractive indices of the layers. The electric field in layer j can be given by[27]

$$E_j(x,z) = (A_j^+ e^{ik_{z,j}z} + A_j^- e^{ik_{z,j}z})e^{i(\omega t - k_{x,j}x)} \tag{4}$$

$$= (U_j^+(z) + U_j^-(z))e^{i(\omega t - k_{x,j}x)}, \tag{5}$$

where $k_{x,j}$ and $k_{z,j}$ are x and z components of the wave vectors in the medium j, respectively, $+$ or $-$ indicates the corresponding direction of wave vectors in the z axis,

$$k_{z,j} = k_j \sin\alpha_{i,j} = k\sqrt{\alpha_i^2 - 2\delta_j - 2i\beta_j}, \tag{6}$$

where the real term of the refractive index $(1-\delta)$ is slightly less than unity and β is the imaginary term of the refractive index of x ray. $U_j^\pm(z)$ are amplitudes of electric fields $+$ or $-$ directions in the layer j as a function of z. The x-ray beam refracts or reflects at the j and $j+1$ interface with the refraction matrix $\mathbf{R}_{j,j+1}$,

$$\mathbf{R}_{j,j+1} = \begin{pmatrix} p_{j,j+1} & m_{j,j+1} \\ m_{j,j+1} & p_{j,j+1} \end{pmatrix}, \tag{7}$$

where

$$p_{j,j+1} = \frac{k_{z,j} + k_{z,j+1}}{2k_{z,j}}, \tag{8}$$

$$m_{j,j+1} = \frac{k_{z,j} - k_{z,j+1}}{2k_{z,j}}. \tag{9}$$

In a layer j with an altitude h, the x ray is transmitted with the translation matrix $\mathbf{T}_j$,

$$\mathbf{T}_j = \begin{pmatrix} e^{-ik_{z,j}h} & 0 \\ 0 & e^{ik_{z,j}h} \end{pmatrix}. \tag{10}$$

Using those refraction and translation matrices, the transfer matrix $\mathbf{M}$ is conveniently introduced to calculate the amplitudes of electric fields,

$$\begin{pmatrix} U_j^+(0) \\ U_j^-(0) \end{pmatrix} = \mathbf{R}_{0,1}\mathbf{T}_1\mathbf{R}_{1,2}\mathbf{T}_2\cdots\mathbf{R}_{sub-1,sub}\begin{pmatrix} U_j^+(z_{sub}) \\ U_j^-(z_{sub}) \end{pmatrix} \tag{11}$$

$$= \mathbf{M}\begin{pmatrix} U_j^+(z_{sub}) \\ U_j^-(z_{sub}) \end{pmatrix}. \tag{12}$$

The ratio of the transfer matrix components M_{12}/M_{22} gives reflectivity under the condition that $U_j^+(z_{sub})=0$.

Using those formula, one can calculate the amplitudes of electric fields in any part of the film. In our particular case, we use a three layer model of ambient, polymer layer, and silicon substrate. Our interest is in the polymer layer, in which scatters are distributed. We use the same derivation of scattering intensities as described by Lee *et al.*[14] and omit the detailed discussion. In the polymer layer, we write the electric field of the incoming wave $\Psi_i(\mathbf{r})$ and its time reversal state (a scattered wave) $\Psi_f(\mathbf{r})$ in unperturbed state,

$$\Psi_i(\mathbf{r}) = e^{i\mathbf{k}_\parallel \cdot \mathbf{r}_\parallel}(T_i e^{ik_{z,i}z} + R_i e^{-ik_{z,i}z}),$$

$$\Psi_f(\mathbf{r}) = e^{i\mathbf{k}_\parallel \cdot \mathbf{r}_\parallel}(T_f^* e^{ik_{z,f}^*z} + R_f^* e^{-ik_{z,f}^*z}). \tag{13}$$

T_i and R_i and their conjugates, and T_f^* and R_f^* are computed with the transfer matrix. The subscript $\parallel$ indicate the component parallel to the substrate. We use the above unperturbed electric fields to calculate the scattering intensity in the presence of scatters (small perturbation) in the polymer layer. We write the amplitude of the wave,

$$\Psi_{sc}(r) = e^{ik_0r}/(4\pi r)[T_iT_fF(q_y,q_{a,z}) + T_iR_fF(q_y,q_{b,z})$$
$$+ R_iT_fF(q_y,q_{c,z}) + R_iR_fF(q_y,q_{d,z})],$$

where, $q_{a,z} = k_{z,f} - k_{z,i}$, $q_{b,z} = -k_{z,f} - k_{z,i}$, $q_{c,z} = k_{z,f} + k_{z,i}$, and $q_{d,z} = -k_{z,f} + k_{z,i}$. $F(q_y,q_{w,z})$ ($w=a,b,c,$ or d) are the form factors of the scatters in the polymer layer. GISAXS intensity I can then be computed with the amplitude and its conjugate $\Psi_{sc}^*(r)$,

$$I(q_y,q_z) = r^2\{\Psi_{sc}(r)\Psi_{sc}^*(r)\} \tag{14}$$

$$= \frac{1 - e^{-2\,\mathrm{Im}(q_z)}}{32\pi^2\,\mathrm{Im}(q_z)}|T_iT_fF(q_y,\mathrm{Re}(q_{a,z}))$$
$$+ T_iR_fF(q_y,\mathrm{Re}(q_{b,z}))$$
$$+ R_iT_fF(q_y,\mathrm{Re}(q_{c,z})) + R_iR_fF(q_y,\mathrm{Re}(q_{d,z}))|^2 \tag{15}$$

$$= \frac{1 - e^{-2\,\mathrm{Im}(q_z)}}{32\pi^2\,\mathrm{Im}(q_z)}[|T_iT_f|^2I(q_y,\mathrm{Re}(q_{a,z}))$$
$$+ |T_iR_f|^2I(q_y,\mathrm{Re}(q_{b,z})) + |R_iT_f|^2I(q_y,\mathrm{Re}(q_{c,z}))$$
$$+ |R_iR_f|^2I(q_y,\mathrm{Re}(q_{d,z}))] + I_{cross} \tag{16}$$

$$= I_{T_iT_f} + I_{T_iR_f} + I_{R_iT_f} + I_{R_iR_f} + I_{cross}. \tag{17}$$

$q_{w,z}$ has an imaginary term when the incident or exit angle is less than or close to the critical angle. The imaginary terms were excluded from the form factor F as in Eq. (15). T and R represent transmitted and reflected waves, respectively. For example, T_iR_f indicates that the transmitted incident wave is scattered and then reflected by the substrate. We use four
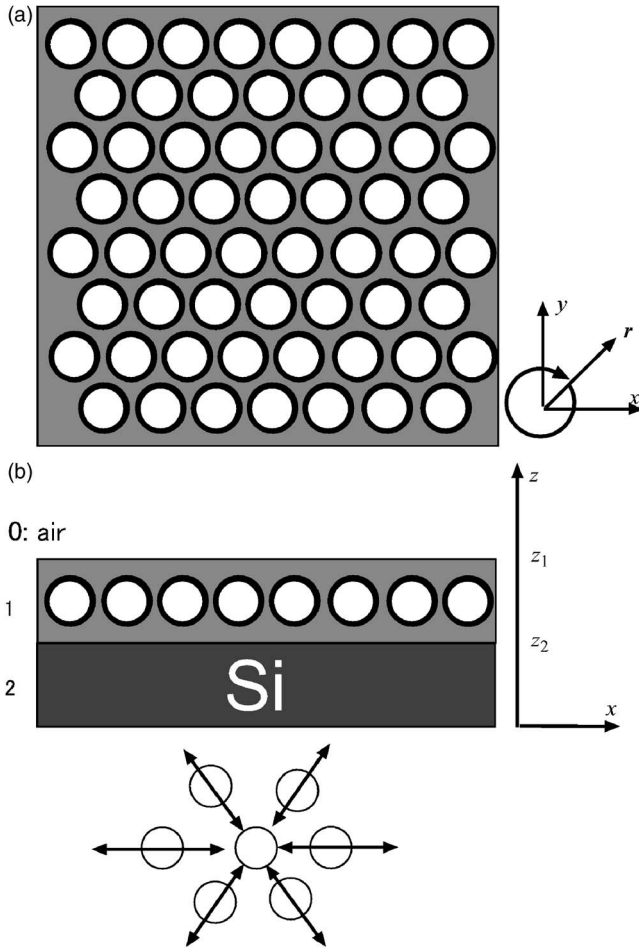
FIG. 3. A model for distorted wave Born approximation. Uniform cells of radius r are packed in a hexagonal lattice as in panel a with paracrystal distortion in panel b. The axes are defined the same way as in Fig. 2.

scattering events, T_iT_f, T_iR_f, R_iT_f, and R_iR_f, to calculate the GISAXS intensities. Equation (15) will be used to obtain the total intensity, but the intensities of four scattering events excluding the cross term in Eq. (16) will also help us to know which scattering event dominates the total intensity.

2. Form and structure factors

We assume that the centers of scatters are in the same plane and are ordered in hexagonal lattice with paracrystal distortion as shown in Fig. 3. A single layer of empty cells in the middle of a 58-nm-thick film has been found in our previous SEM study.[4] Therefore, it is reasonable to start from assuming a single layer model for the DWBA analysis. We will introduce the structure factor of such lattice in the x-y plane later in this section.

Let us first introduce a form factor of individual scatters. We employ two shapes of scatters: spheres (S) and spherical concentric shells (SCS). S model has spherical empty cells with an average radius R_i and have a Gaussian distribution with a standard deviation of δ_{R_i}. The amplitude of a form factor of low scattering density spheres in a high scattering density medium (empty cells) is the same as that of high scattering density spheres in a low scattering medium (particles). A SCS model is defined with inner R_i and outer R_o

radii with a Gaussian distribution of R_i with a standard deviation of δ_{R_i}. Distribution is introduced only into R_i. When a radius R is $R<R_i$, scattering density is assumed to be zero. In the shell ($R_i<R<R_o$), PFMA with δ_{PFMA} and β_{PFMA} occupies. In the matrix ($R_o<R$), PS with δ_{PS} and β_{PS} occupies. Such SCS models are expected from the mechanism of nanocellular formation that has not been experimentally confirmed.

The form factors for S and SCS models have been analytically provided.[28] For spherical scatters including spherical empty cells, the amplitude of the form factor of a sphere $F_s(q)$ with a radius R is given by[28]

$$F_S(q,R) = \frac{3[\sin(qR) - qR\cos(qR)]}{(qR)^3}. \tag{18}$$

An amplitude of a form factor of spherical concentric shells is given by[28]

$$F_{SCS}(q,\{R_k\}) = \frac{1}{M}\Bigg[\rho_1 V(R_1) F_S(q,R_1) + \sum_{k=2}^{N} (\rho_k - \rho_{k-1}) V(R_k) F_S(q,R_k) \Bigg], \tag{19}$$

where ρ and V are the scattering density and volume, respectively. $\{R_k\}$ represents a set of radii to define the SCS model. M is the scattering volume of the scatter given by

$$M = \rho_1 V(R_1) + \sum_{k=2}^{N} (\rho_k - \rho_{k-1}) V(R_k). \tag{20}$$

In our case, the media 1, 2, and 3 correspond to air, PFMA, and PS, respectively. $\delta_{PS}=3.45\times10^{-6}$, $\delta_{PFMA}=5.00\times10^{-6}$, $\delta_{Si}=7.43\times10^{-6}$, $\beta_{PS}=5.24\times10^{-9}$, $\beta_{PFMA}=2.40\times10^{-8}$, and $\beta_{Si}=1.72\times10^{-7}$ are used for the computation of the scattering intensities. The total scattering intensities are expressed as the sum of four waves in Eq. (15) and can be computed with the form factors $F_S(q,R_i)$ and $F_{SCS}(q,R_i,R_o)$. In addition, Gaussian distribution $g_r(r)$ with a standard deviation σ_{R_i} as a fitting parameter for S and SCS models was introduced. In the case of SCS, R_o was assumed not to be correlated to R_i and chosen independently. We rewrite the intensity in Eq. (15) as $I(\mathbf{q},r)$. $I(\mathbf{q},r)$ is the GISAXS intensity for monodispersed inner radius r. We define the total GISAXS intensity from a polydispersed system by assuming the local monodisperse approximation,

$$I_{poly} = \int g_r(r)v(r)^2 I(\mathbf{q},r)dr, \tag{21}$$

where $v(r)$ and $g_r(r)$ are the volume of the sphere with radius r and a Gaussian distribution, respectively,

$$g_r(r) = \frac{1}{\sigma_{R_i}\sqrt{2\pi}} \exp\left(-\frac{(r-R_i)^2}{2\sigma_{R_i}^2} \right). \tag{22}$$

R_i and σ_{R_i} are mean and standard deviation of radius r.

The derived scattered intensity I_{poly} is for randomly distributed uncorrelated S and SCS. We need to introduce an intercell correlation of hexagonally packed S or SCS in a

layer. Since the hexagonal symmetry is not originated from the interaction of the cells but from the ordered structure of the original block copolymer template, we assume that the hexagonal lattice is independent from the size of cells. The structure factor for two dimensional (2D) hexagonal can be calculated by Fourier transform of a complete set of lattice points. We also introduce the imperfectness of the hexagonal lattice in the model by employing paracrystal distortion.[6,14,29] As indicated in Fig. 3, paracrystal distortion was introduced without disturbing the sixfold symmetry. The structure factor $S(\mathbf{q})$ can be calculated as follows:[14]

$$S(\mathbf{q}) = \prod_{k=1}^{3} Z_{p,k}(\mathbf{q}), \quad (23)$$

where

$$Z_{p,k}(\mathbf{q}) = 1 + \frac{F_{p,k}(\mathbf{q})}{1 - F_{p,k}(\mathbf{q})} + \frac{F_{p,k}^{*}(\mathbf{q})}{1 - F_{p,k}^{*}(\mathbf{q})}, \quad (24)$$

$$F_{p,k}(\mathbf{q}) = e^{-(1/2)\sigma_{b_k}^2 q^2} e^{-i\mathbf{q}\cdot b_{\mathbf{k}}}. \quad (25)$$

$\mathbf{b_k}$ and σ_{b_k} are the fundamental vectors and their displacements. In the case of 2D hexagonal lattice in randomly oriented polygrains, the structure factor can be simplified to $S(q_y, L)$, where L is a scalar fundamental lattice distance. $S(q_y, L)$ does not depend on q_z, and hence the GISAXS intensity from the hexagonal ordered system can be rewritten as

$$I_{\text{poly,ordered}} = S(q_y, L) I_{\text{poly}}. \quad (26)$$

Finally we assume that the scattering intensity can be obtained from the in-plane azimuthal average[6] of this model to account for the randomly oriented polygrain structure.

III. RESULTS AND DISCUSSION

A. GISAXS experiment

A thin film of a mixture of PS-PFMA and low molecular weight homo-PS was processed with CO_2 to introduce nanocells. The mixture was used instead of pure PS-PFMA since adding low molecular weight homo-PS enhanced the monodispersity of cells and the degree of order in our previous study.[4] It is apparently due to the thickened PS walls by the added homo-PS that separate the cells and hence stabilize the cell size upon depressurization. An example of GISAXS patterns of the films after thermal annealing (130 °C for 12 h) (a) and the CO_2 process (b) at an incident angle α_i of 0.15° are shown in Fig. 4. The GISAXS pattern from the thermally annealed PS-PFMA thin film shows two peaks on the Yoneda wing,[30] which is diffused scattering from the film surface appearing as a horizontal line. In this particular case, two Yoneda wings appear at two values of q_z that correspond to the critical angles of reflection of PS-PFMA surface and silicon surface. Bragg diffraction from the block copolymer domains appears only on the Yoneda wings, which indicates that the domain structure is ordered only in the x-y plane. However, higher order diffraction is not observed and hence the structure is only short range ordered in the thermally annealed film. The PS-PFMA block copolymer used in this
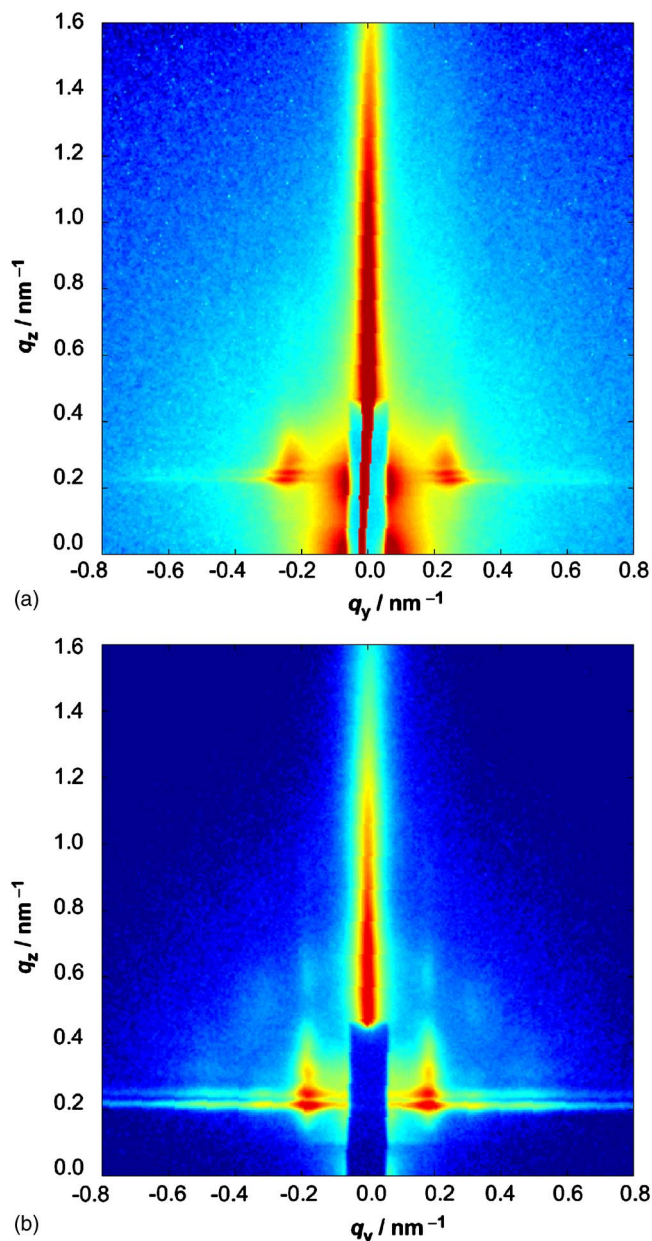

FIG. 4. Examples of GISAXS patterns from PS-PFMA block copolymer thin films on silicon substrate after thermal annealing (a) and after the CO_2 process (b). Incident angle α_i of 0.15° was chosen. Intensity increases from blue to red in logarithmic scale.

experiment forms spherical domains as previously reported[1–4] although the block fraction of PFMA is rather high for spherical domains. With the thickness range of 50–70 nm, PFMA spheres are expected to align in a single layer on a flat substrate. The GISAXS pattern confirms the formation of a single layer. However, the GISAXS pattern lacks unique features of the form factor of the PFMA domains probably due to a large size distribution. The poor long range order of this thermally annealed PS-PFMA is primarily due to the strong interaction between PS and PFMA, which restricts the reorganization.[31]

In Fig. 4(b), the GISAXS pattern from the nanocellular thin film after the CO_2 process is shown. To avoid saturation of the CCD detector, the exposure times for thermally annealed and CO_2 processed films were set to 10 and 0.2 s,
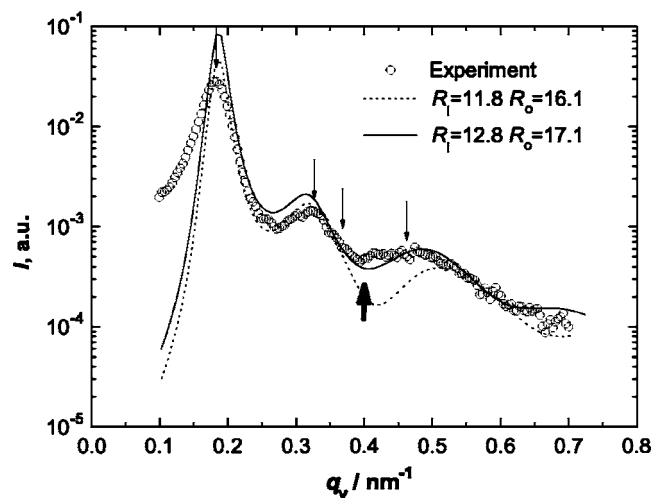
FIG. 5. Intensity vs q_y of the nanocellular thin film at the critical q_z of the nanocellular film. The thin arrows are 1, $\sqrt{3}$, $\sqrt{4}$, and $\sqrt{7}$ relative to the first order. The thick arrow is the first fringe of the form factor.

FIG. 6. Intensity vs q_z of the nanocellular thin film at the peak q_y.

respectively. The peak intensities at the Bragg peaks of the two GISAXS patterns have nearly the same intensities, but the background levels differ greatly. It indicates that the scattering intensity from the CO_2 processed film is at least ten times higher than the thermally annealed film. That is a strong evidence of the presence of the empty nanocells, which bring greater contrast for x ray in the CO_2 processed film as previously reported.[1–4] In addition, the GISAXS pattern in Fig. 4(b) shows more recognizable features than that of the thermally annealed PS-PFMA film in Fig. 4(a): (1) presence of higher order peaks on the Yoneda wings; (2) circular fringes (weak intensity circular lines); (3) vertical oscillating streaks at q_y of the first order peak ($q_{y,max}$); and (4) Bragg peaks appearing only on the Yoneda wings, which indicate that the ordering is restricted in the plane. Therefore, the cells form a single layer in the film. The Yoneda wings in Fig. 4(b) are separated further than those in Fig. 4(a). The larger separation is primarily due to the reduced electron density of the nanocellular films with air. The reduction of the critical angle will be discussed later in this paper.

Let us first focus on the in-plane structure of the nanocellular film. The GISAXS intensity along q_y axis at the critical q_z of the nanocellular thin film after the CO_2 process is plotted in Fig. 5. The lattice dimension $2\pi/q_{y,max}$ of 34.2 nm estimated from the first order peak of CO_2 processed film is significantly larger than 25.7 nm of the thermally annealed film. If the block copolymer domain structure works as a simple template, the lattice dimension should be unchanged. This problem has been recognized in our previous AFM and SEM studies,[4] in which the number density of cells in the film with a single layer of domains/cells changed after the process. GISAXS statistically reconfirmed the same trend. The spherical domains or cells are in a single layer, and the films can expand only to the z axis. The only way to change the lattice dimension or equivalently the number density of spherical domains or cells upon swelling is to reorganize the block copolymer chains and to reassemble the spherical domains or cells. The increasing lattice dimension suggests that, during the CO_2 process, PS-PFMA chains reduce the
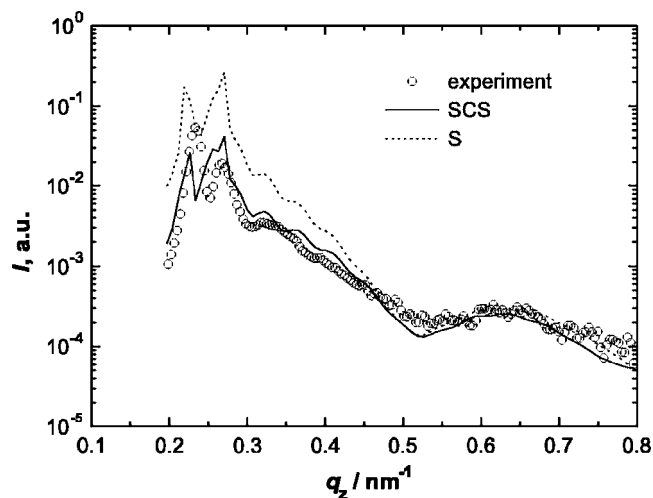
number of aggregates (reduce the number density and increase the lattice dimension) to accommodate the absorbed CO_2. In thermal annealing, the diffusion and reorganization of the structure is strongly restricted by the strong interaction between PS and PFMA,[31] but the reorganization can be enhanced in the CO_2 process since CO_2 reduces the effective interaction between PS and PFMA and accelerates the diffusion of PS-PFMA copolymer molecules.

In addition to the intense first order peaks, the higher order peaks are found in Fig. 5. The positions of the arrows are 1, $\sqrt{3}$, 2, and $\sqrt{7}$ relative to the first order. 1 and $\sqrt{3}$ peak positions of the hexagonal lattice agree very well with the experiment while $\sqrt{4}$ and $\sqrt{7}$ suffer from overlapping with the form factor of the scatters. The reasonable agreement of the positions is an indication of hexagonal symmetry. Since the Bragg peaks are only in the x-y plane, the structure of the cells is 2D hexagonal. It should be noted that hexagonal symmetry is not clearly observed in the thermally annealed films of the same copolymer. The broad peak that appeared at $q_y=0.5$ nm^{-1} with characteristic fringe at 0.4nm^{-1} is not due to the interference function of the lattice but a typical character of an intrascatter form factor. Evidently, the fringe that appeared at 0.4nm^{-1} in Fig. 5 is a part of the circular pattern that appeared in the y-z plane in Fig. 4(b) and hence is distinguished from the interference function of the lattice confined in the film plane. In traditional transmission SAXS experiments of ordered but randomly oriented block copolymer domains, a form factor often overlaps with the structure factor of the lattice. However, aligning block copolymer domains in thin film and employing GISAXS experiments effectively separate the form factor of domains from the structure factor of the lattice.

Let us examine a slice along the z axis of Fig. 4(b). This z slice contains the information primarily from the depth direction of the film similar to specular reflectivities. The z slice of the profile at $q_{y,max}$ is plotted in Fig. 6. Two strong peaks in the low q_y region ($0.2 < q_z < 0.3$) are characteristics of the critical angles of reflection of the nanocellular film and silicon substrate. Since the nanocellular thin film is supported on a silicon substrate and the x ray is reflected at both the film and substrate surfaces, the Yoneda peak splits into

TABLE II. Model parameters for DWBA calculation.

Model	R_i	R_o	σ_{R_i}	L	σ_L	Thickness	Porosity
Sphere (S)	10.2	$\cdots$	0.95	37.2	0.80	67.0	0.111
Spherical concentric shell z (SCS$_z$)	11.8	16.1	0.86	37.2	0.80	67.0	0.174
Spherical concentric shell y (SCS$_y$)	12.8	17.1	1.15	37.2	0.80	67.0	0.219

the two peaks. As q_z increases, the intensity decays with small oscillations and then shows a distinct fringe and a broad peak similar to the y slice in Fig. 5. The fringe at q_z of 0.53 nm^{-1} is a part of the form factor fringes that appeared as a ring pattern in Fig. 4(b). The appearance of the form factors in y and z slices is qualitatively the same, but the structure factor of the lattice is excluded in the z slice.

In order to analyze the GISAXS pattern quantitatively, computation with a model using DWBA is required. The background of DWBA and the model have been introduced in the previous section. First, we compare the z slice of the GISAXS pattern and the computed intensities using S and SCS models. Parameters used to simulate the experimental pattern are given in the Table II. We adopted a full DWBA calculation with the cross term for the fitting, but omitting the cross term did not change the global scattering intensity pattern except the disappearance of small fringes.

First of all, we fit the experimental profile with the S model. The radius of the sphere was chosen so that the fringe of the form factor of the computation fits the experimental profile. The parameters used for the fit are given in Table II as S and the result of the computation with the parameters is drawn with the dotted line in Fig. 6. The thickness used for the model was independently measured by ellipsometry. As clearly found in Fig. 6, the computation cannot fit the low and high q_z regions simultaneously. The choice of all the other parameters did not improve the fit to the experiment. It is suspected that the use of the form factor of a sphere is too much simplification. According to the proposed mechanism of introduction of empty cells, CO_2 is introduced into the CO_2-philic PFMA domains. If it is the case, the empty cells are surrounded by the PFMA domains with the higher scattering density in the matrix of PS with the lower scattering density as schematically drawn in Figs. 1 and 3. To describe such structure, SCS model is introduced. The form factor of the SCS model has been given in Sec. II. The SCS model with the parameters given as SCS$_z$ in Table II provides a reasonable fit to the experiment in all q_z range as shown as a solid line in Fig. 6. In addition to our previous indirect proof[32] of nanocells surrounded with CO_2-philic domains, this successful fit of spherical concentric shell model to the GISAXS profile is an evidence of nanocellular formation mechanism in which CO_2 localizes in CO_2-philic domains and make cells upon depressurization.

In order to check the validity and consistency of the SCS model and the parameters, the same parameters are also applied for the y slice. Simulated profiles are overlaid in Fig. 5 as a dotted line. The parameters obtained from the best fit of the z slice does not satisfactory fit the data in the y slice. Even larger value of R_i tabulated in Table II as SCS$_y$ is necessary to fit the experimentally observed profile. How-

ever, the difference of the radii of SCS$_z$ and SCS$_y$ is only 10%. For the y slice, the interference of the form factor and the structure factor of the hexagonal lattice is not completely negligible. The first fringe of the form factor is interfered with $\sqrt{7}$ peak of the structure factor of the hexagonal lattice. Moreover, the radii estimated from the z slice have an error of 10% or less as will be discussed later. It should also be noted that σ_{R_i} is approximately 1 nm, which is small enough for this form factor analysis, but still brings approximately 10% of size distribution. Under such circumstances, we conclude that the cells are spherical and no significant difference of the cell shape in the depth and in-plane directions. The GISAXS patterns from pure PS-PFMA thin films with the same CO_2 process was also obtained, but showed featureless scattering pattern other than the intense Bragg peaks from the lattice. Such result is due to the large size distribution, and quantitative further analysis of the form factor using the calculation with DWBA is not feasible.

Considering the change of thickness (51–67 nm) measured by ellipsometry with introduced cells, the porosity of the film is estimated to be 24%, which is slightly larger than the values obtained by the SCS model, but significantly deviates from the value of the S model. This comparison of porosities also suggests that the SCS model represents the structure of the film better than the S model.

The double peaks between 0.2 and 0.3 in the z slice of Fig. 6 are due to the critical angles of reflections of the nanocellular film and silicon as already mentioned. The DWBA calculation shows similar peaks at approximately the same q_z although the intensities do not quantitatively agree with each other. The intensity at this angle may contain the scattering from the surface roughness of the nanocellular thin film and silicon wafer, which makes quantitative prediction difficult. Actually, the peak intensity of the critical angle of the nanocellular film relative to the peak for silicon wafer surface in the experiment is stronger while DWBA calculation predicts rather opposite result. This result may suggest that the surface of the nanocellular film is slightly rougher than an ideally smooth surface. The peak positions in q_z of Yoneda wings are strongly influenced by the porosity of the film since the porosity alters the effective refractive index (scattering density) of the film and its critical angle of reflection. The porosity of the film given in Table II is not a free fitting parameter but is calculated from the radius of the cells and lattice dimension. Nevertheless, the peak position of the critical angle of the nanocellular film calculated from the model agrees reasonably well with the experiment, which supports the validity of the model and parameters for the nanocellular thin film.
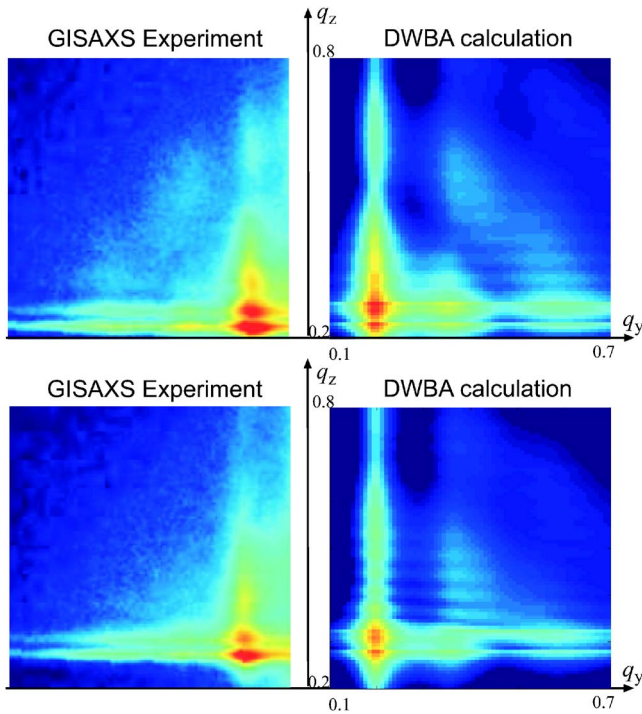
FIG. 7. Calculated and measured two dimensional intensity images at incident angles of 0.150° and 0.225°.

FIG. 8. Calculated intensities using DWBA of the z slices at the $q_{y,max}$, q_y with a maximum intensity, at incident angles of 0.150° (above) and 0.225° (below). Full calculation of DWBA (solid) and its components: T_i and R_f are transmitted and reflected components, respectively. For instance, $R_i T_f$ indicates that the incident x ray was reflected, scattered, and transmitted through the sample and reached the detector.

The computed and experimentally obtained 2D GISAXS patterns are shown in Fig. 7. In both calculated and experimental 2D patterns, circular ring of weak intensity fringes, which correspond to the form factors of spherically concentric shells, are found at the incident angle of 0.150°. However, for the incident angle of 0.225°, no clear evidence of the circular form factor is found. Why is the form factor sensitive to the choice of incident angle? In the series of GISAXS patterns from 0.050° to 0.250°, the clear circular form factors are found only a few choices of the incident angles. As explained in Sec. II, GISAXS intensities are approximated by four scattering events as shown in Eq. (16): (1) transmitted x ray is scattered and transmitted ($T_i T_f$); (2) transmitted x ray is scattered and reflected ($T_i R_f$); (3) reflected x ray is scattered and transmitted ($R_i T_f$); and (4) reflected x ray is scattered and reflected ($R_i R_f$). All four waves add to the total intensity. In the case of sharp Bragg peaks, peak positions are not altered by the interference of four scattering events. However, the gradually changing fringes of the form factors may interfere one another when the intensities of scattering events are comparable. For example, we show in Fig. 8 the calculated z slice of the total GISAXS intensity of Eq. (15) with the intensities of all four scattering events of Eq. (16) at incident angles of 0.150° and 0.225°. The total intensity was calculated with Eq. (15), which includes the cross term (interference) between the four scattering events and hence shows the small oscillation due to the interference of $T_i T_f$ and $R_i T_f$ waves. In the case of the incident angle of 0.150°, the total intensity is dominated by the $R_i T_f$ event and the position of the first fringe of the form factor of $R_i T_f$ corresponds to the fringe appearing in the GISAXS pattern. In addition, $T_i T_f$ is very similar to $R_i T_f$. Even when $T_i T_f$ were the dominating event, the scattering
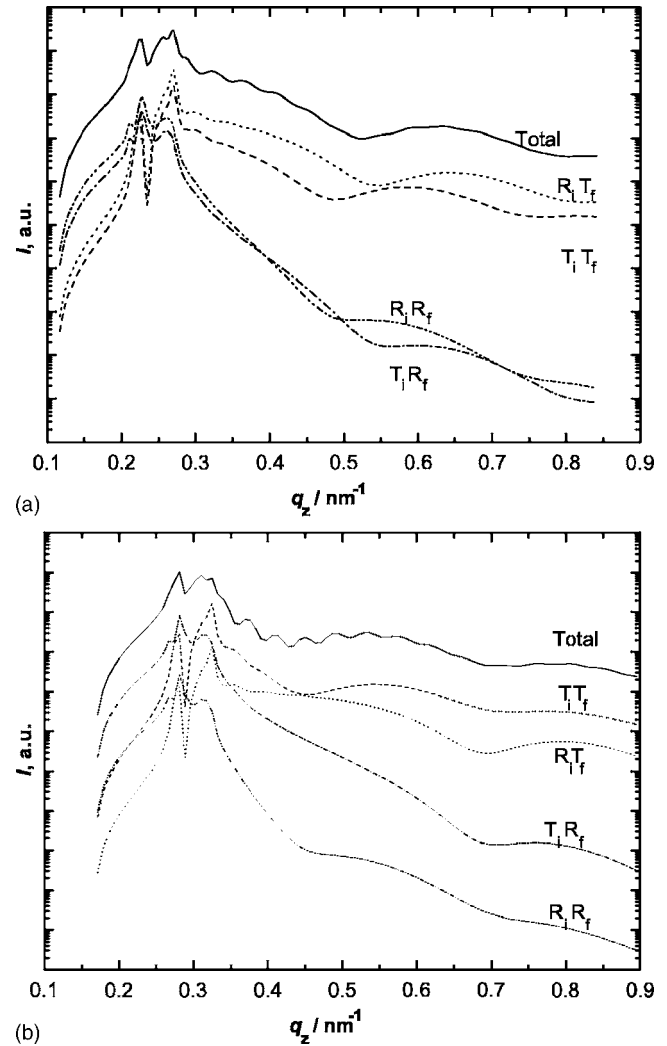
profile would be qualitatively the same and the size of cells would be underestimated by 10%. At 0.150° of incident, which is close to but above the critical angle of reflection, the refracted x ray is nearly parallel to the film plane and is totally reflected at the silicon surface; therefore, the difference between $T_i T_f$ and $R_i T_f$ is small. Such a choice of incident angle enhances the appearance of the form factor of the embedded scatters.

On the other hand, in the case of the incident angle of 0.225°, the total intensity is dominated by the $T_i T_f$ event and the $R_i T_f$ profile significantly differs. The uncertainty of the relative intensity of the scattering events may alter the result of the analysis. In addition, the first fringe of the form factor is close to the critical angle of reflection of silicon. Note that the scattering from the form factor is totally eliminated below the critical angle of silicon. In order to observe a clear circular pattern of the first fringe of the form factor, there is not enough separation between the Yoneda peak and the first fringe in the case of the incident angle of 0.225°. In fact, in

Fig. 7, no clear circular pattern was observed either in the experiment nor DWBA calculation. In order to analyze a form factor of scatters embedded in a thin film, an incident angle must be carefully chosen so that the characteristic fringe of the form factor does not suffer from the interference between four different scattering events. Without the detailed analysis using DWBA, it is difficult to evaluate the apparent form factors in GISAXS patterns.

IV. CONCLUSION

We analyzed the shape and size of the nanocellular structures fabricated using a block copolymer template with the help of carbon dioxide process. Grazing incident small angle x-ray scattering (GISAXS) successfully probed the embedded nanostructures. Nanocells are ordered in 2D hexagonal lattice as a single layer in thin films and are surrounded by the CO_2-philic PFMA domains in the matrix of PS. Their spacing, average size, and distribution were analyzed by comparing the form and structure factors of the DWBA calculation and GISAXS experiments. However, due to the complex reflection/refraction of incident and scattered x rays, quantitative evaluation of the form factors can be achieved only when the apparent form factor is dominated by one of four scattering events in the calculation with DWBA. To do so, a proper choice of experimental condition such as incident angle accompanied with the calculation using DWBA is essential.

ACKNOWLEDGMENTS

[1] H. Yokoyama, L. Li, T. Nemoto, and K. Sugiyama, Adv. Mater. (Weinheim, Ger.) **16**, 1542 (2004).
[2] H. Yokoyama and K. Sugiyama, Macromolecules **38**, 10516 (2005).
[3] L. Li, H. Yokoyama, T. Nemoto, and K. Sugiyama, Adv. Mater. (Weinheim, Ger.) **16**, 1226 (2004).
[4] L. Li, T. Nemoto, K. Sugiyama, and H. Yokoyama, Macromolecules **39**, 4746 (2006).
[5] B. Mahltig, P. Muller-Buschbaum, M. Wolkenhauer, O. Wunnicke, S. Wiegand, J. F. Gohy, R. Jerome, and M. Stamm, J. Colloid Interface Sci. **242**, 36 (2001).
[6] R. Lazzari, J. Appl. Crystallogr. **35**, 406 (2002).
[7] P. Muller-Buschbaum, Anal. Bioanal. Chem. **376**, 3 (2003).
[8] A. Gibaud, A. Baptiste, D. A. Doshi, C. J. Brinker, L. Yang, and B. Ocko, Europhys. Lett. **63**, 833 (2003).
[9] A. Gibaud, D. Grosso, B. Smarsly, A. Baptiste, J. F. Bardeau, F. Babonneau, D. A. Doshi, Z. Chen, C. J. Brinker, and C. Sanchez, J. Phys. Chem. B **107**, 6114 (2003).
[10] A. Gibaud, S. Dourdain, O. Gang, and B. M. Ocko, Phys. Rev. B **70**, 161403 (2004).
[11] T. Xu, J. T. Goldbach, M. J. Misner *et al.*, Macromolecules **37**, 2972 (2004).
[12] I. Park, B. Lee, J. Ryu, K. Im, J. Yoon, M. Ree, and T. Chang, Macromolecules **38**, 10532 (2005).
[13] B. Lee, W. Oh, Y. Hwang, Y. H. Park, J. Yoon, K. S. Jin, K. Heo, J. Kim, K. W. Kim, and M. Ree, Adv. Mater. (Weinheim, Ger.) **17**, 696 (2005).
[14] B. Lee, I. Park, J. Yoon, S. Park, J. Kim, K. W. Kim, T. Chang, and M. Ree, Macromolecules **38**, 4311 (2005).
[15] B. Lee, W. Oh, J. Yoon, Y. Hwang, J. Kim, B. G. Landes, J. P. Quintana, and M. Ree, Macromolecules **38**, 8991 (2005).
[16] B. Lee, J. Yoon, W. Oh, Y. Hwang, K. Heo, K. S. Jin, J. Kim, K. W. Kim, and M. Ree, Macromolecules **38**, 3395 (2005).
[17] Z. Sun, M. Wolkenhauer, G. G. Bumbu, D. H. Kim, and J. S. Gutmann, Physica B **357**, 141 (2005).
[18] A. Gibaud, S. Dourdain, and G. Vignaud, Appl. Surf. Sci. **253**, 3 (2006).
[19] B. D. Lee, Y. H. Park, Y. T. Hwang, W. Oh, J. Yoon, and M. Ree, Nat. Mater. **4**, 147 (2005).
[20] J. Yoon, S. Y. Yang, K. Heo, B. Lee, W. Joo, J. K. Kim, and M. Ree, J. Appl. Crystallogr. **40**, 305 (2007).
[21] K. Heo, K. S. Oh, J. Yoon, K. S. Jin, S. Jin, C. K. Choi, and M. Ree, J. Appl. Crystallogr. **40**, s614 (2007).
[22] J. Yoon, S. Choi, S. Jin, K. S. Jin, K. Heo, and M. Ree, J. Appl. Crystallogr. **40**, s669 (2007).
[23] K. Sugiyama, T. Nemoto, G. Koide, and A. Hirao, Macromol. Symp. **181**, 135 (2002).
[24] H. Okuda, S. Ochiai, K. Ito, and Y. Amemiya, Appl. Phys. Lett. **81**, 2358 (2002).
[25] S. K. Sinha, E. B. Sirota, S. Garoff, and H. B. Stanley, Phys. Rev. B **38**, 2297 (1988).
[26] M. Rauscher, T. Salditt, and H. Spohn, Phys. Rev. B **52**, 16855 (1995).
[27] A. Gibaud and S. Hazra, Curr. Sci. **78**, 1467 (2000).
[28] J. S. Pedersen, Adv. Colloid Interface Sci. **70**, 171 (1997).
[29] B. Busson and J. Doucet, Acta Crystallogr., Sect. A: Found. Crystallogr. **56**, 68 (2000).
[30] Y. Yoneda, Phys. Rev. **131**, 2010 (1963).
[31] H. Yokoyama, Mater. Sci. Eng., R. **53**, 199 (2006).
[32] L. Li and H. Yokoyama, Angew. Chem., Int. Ed. **45**, 6338 (2006).